metals

MDPI

Article

Effect of Feature Size on Defects, Microstructure, and Mechanical Properties of Selective Laser Melted AlSi10Mg Lattice Structure

Chengkuan Peng [1], Junfeng Qi [1,*], Sheng Zhou [2], Sanqiang Yang [1,3], Ran Tao [2], Heng Shao [1] and Weining Li [1]

[1] Beijing Spacecraft Manufacturing Co., Ltd., China Academy of Space Technology, Beijing 100094, China; chengkuanpeng@163.com (C.P.); sq.yang@stu.pku.edu.cn (S.Y.); shao_heng@126.com (H.S.); chaoqwe2@126.com (W.L.)
[2] Institute of Advanced Structure Technology, Beijing Institute of Technology, Beijing 100081, China; 3220222294@bit.edu.cn (S.Z.); taoran@bit.edu.cn (R.T.)
[3] College of Engineering, Peking University, Beijing 100871, China
* Correspondence: qjfcn@163.com

Abstract: Selective laser melting lightweight lattice structures have broad application prospects in the aerospace field. Understanding the dependence of mechanical performance on feature size is crucial for structure design. This work optimized the process parameters based on large-size metal blocks (20 mm) and then fabricated submillimeter features with a size of 0.4~1.0 mm. The influence of feature size on the defects, microstructures, and mechanical properties was investigated. The results showed that the dimensional errors for all size features were above 15%. When matched with appropriate border offset, these features could be printed precisely. The densification of submillimeter features was more than 99%, demonstrating the applicability of the optimized process parameters for the fine features. The porosity and relative roughness decreased and tended to stabilize with increasing feature size. Due to having less defects, the thicker features exhibited better mechanical properties in terms of ultimate strength and elongation. After being processed with polishing treatment, the roughness was reduced below 1 μm and the tensile strength increased above 320 MPa. The elastic modulus, yield strength, and elongation were also significantly improved.

Keywords: selective laser melting; lattice structure; size effect; dimensional accuracy; AlSi10Mg

Academic Editor: Abdollah Saboori

Received: 26 November 2024
Revised: 8 January 2025
Accepted: 13 January 2025
Published: 16 January 2025

Citation: Peng, C.; Qi, J.; Zhou, S.; Yang, S.; Tao, R.; Shao, H.; Li, W. Effect of Feature Size on Defects, Microstructure, and Mechanical Properties of Selective Laser Melted AlSi10Mg Lattice Structure. *Metals* **2025**, *15*, 77. https://doi.org/10.3390/met15010077

1. Introduction

A lattice structure is a kind of artificially designed porous material. Unlike randomly distributed metal foam, the cells of the lattice structure are arranged periodically in space [1]. A large number of cavities inside the lattice structure provide feasibility for lightweight design. With the advantages of low density and high specific strength and stiffness, lattice structures are widely used in aerospace fields. The programmable cells can endow the lattice structure with unique physical performance, such as a negative Poisson ratio [2], vibration reduction [3], thermal control [4], electromagnetic shielding [5], and acoustic shielding [6], which do not exist in nature. The combination of outstanding load-bearing capacity and function lays the foundation for the idea of structure–function integration design [7], and greatly promotes the application and development of lattice structures.

The performance of lattice structure depends on their internal complex structure design. Traditional forming and processing technologies are unable to fabricate such intricate structures. The advent of additive manufacturing (AM) technology provides a solution

for the fabrication of cross-scale lattice structures. Ran Tao [8] innovatively integrated lattice structure optimization design and additive manufacturing technology to achieve the efficient structural design and experimental validation of lattice metamaterials. The results showed that AMed lattice metamaterial exhibited excellent performance in energy absorption, load-bearing capability, and thermal management. The innovative work provides strong theoretical and experimental support for the design of future multifunctional materials. Selective laser melting (SLM) is one of the most widely used additive manufacturing techniques [9]. During the printing process, a high-energy laser beam is used to melt the metal powder track by track according to the planned trajectory. Through the overlap between track and track, and layer and layer, the designed model is finally printed. Compared with the traditional process, SLM has higher forming accuracy and can realize the fabrication of submillimeter (<1 mm) features. SLM also has obvious advantages in terms of material utilization and production cycle. The development of SLM technology provides strong technical support for the innovative design and functional exploration of lattice structures [10].

The defects introduced in the SLM process, such as microscopic pores [11–14], surface roughness [15–20], dimensional accuracy [21,22], etc., have significant effects on mechanical performance. The SLM process involves hundreds of process parameters, and a reasonable combination of process parameters is crucial for forming quality control [21,23–28]. In addition to the process parameters, the as-designed model also plays an important role in print quality. Wang et al. [29] used 316L stainless-steel powder to print struts with a diameter ranging from 0.25 mm to 5 mm. It was observed that the distance between the primary dendrite arms of the sub-cell decreased as the diameter of the strut increased from 0.25 mm to 1 mm, and remained stable when the diameter was larger than 1 mm. This difference in microstructure further caused differences in hardness and tensile strength. Dong et al. [30] also observed the influence of geometry size on microstructure in an AlSi10Mg specimen with a diameter of 1~5 mm. As the size increased, there was a transition from fine equiaxed crystals to coarse columnar crystals. Furthermore, the microscopic porosity decreased significantly. As a result, the larger specimen showed a higher yield strength and ultimate tensile strength. Majeed et al. [31] found that the hardness of AlSi10Mg thin-wall structures with different thicknesses was significantly different. The microstructure and defects of Ti6Al4V struts and thin walls are also shaped by geometry size, which will further influence the mechanical properties [32–34]. Shahabad et al. [35] and Promoppatum et al. [36] analyzed the influence of feature size on molten pool size, temperature gradient, and cooling rate through numerical simulations, and explained the influence mechanism on the microstructure.

Among all the metals used for SLM, AlSi10Mg stands out due to its excellent printability, as well as specific stiffness, specific strength, and thermal and electrical conductivity [37,38]. In order to accommodate the requirements of bearing and lightweight in aerospace applications, the diameter of the strut of a lattice structure is usually designed to 0.4~1.0 mm, and the thickness of the external skin is usually less than 1 mm. Up to now, the size effect of AlSi10Mg skin lattice structures has not been fully studied. On the one hand, existing studies mainly focus on scales greater than 1.0 mm, which is higher than the feature size. On the other hand, the influence of porosity, roughness, and microstructure on mechanical properties is complex, and the systematic analysis of the influence mechanism of feature size on mechanical properties needs to be supplemented.

To complement the gaps of current studies, the features of an AlSi10Mg body-centered cubic lattice structure were taken as samples to analyze the influence of size on forming quality. Firstly, the process parameters were optimized and then were used to print features with a size of 0.4~1.0 mm. The as-built size was measured to investigate the effect of

geometry size on dimension accuracy, and appropriate BO was set to compensate for dimensional errors. The defects and microstructure were characterized to analyze the effect of geometry size on the printing quality. After that, the relationship between feature size and mechanical properties was explored. In addition, a polishing treatment was implemented to explore the surface quality in relation to mechanical properties.

2. Materials and Methods

2.1. Materials

AlSi10Mg powder was used, which was supplied by Zhong Yuan Advanced Material Technology Co., Ltd. (Ningbo, China). The tap density was 2.67 g/cm^3 and the apparent density was 1.35 g/cm^3. The SEM image and particle size distribution of the AlSi10Mg powder are shown in Figure 1. The particle size ranges from 20 μm to 63 μm, and D10, D50, and D90 are 25.6 μm, 42.98 μm, and 70.52 μm, respectively. The flow test results showed that the Hall flowability was 75.5 s. The chemical composition was examined according to GB/T 20975 standard [38], and the proportion is shown in Table 1. In addition to three major elements of Al, Si, and Mg, the powder also contained some microelements, such as Fe, Cu, and Ti, and the cumulative proportion of microelements was less than 0.5%.

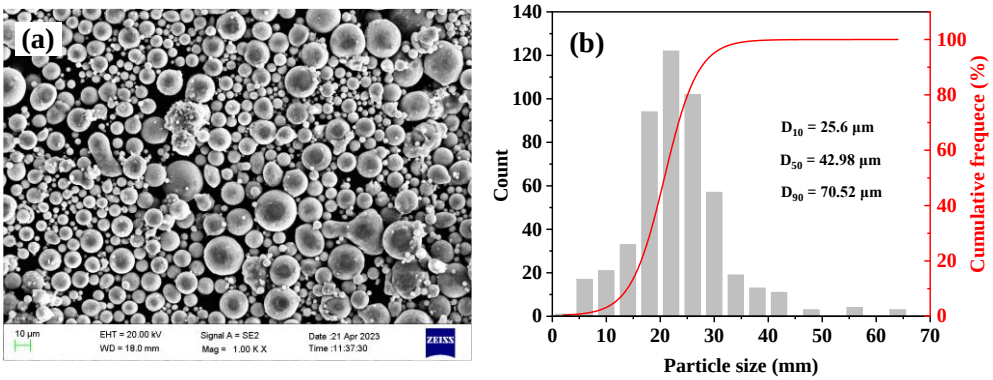

Figure 1. (**a**) SEM image of AlSi10Mg powder; (**b**) powder size distribution.

Table 1. AlSi10Mg powder chemical composition (in wt%).

Element	Si	Mg	Fe	Cu	Mn	Ni	Zn	Ti	Sn	Pb	Al
Composition (wt%)	10.23	0.39	0.16	0.011	0.009	0.01	0.011	0.013	0.011	0.01	Bal

An EP-M650 machine (E-plus 3D Technology Co., Ltd., Beijing, China) was used to fabricate samples. This machine is configurated with a forming chamber of 657 × 657 × 800 mm^3 and is suitable for the formation of large-sized metal parts. To ensure production efficiency, the system is equipped with four lasers and vibroscopes. The maximum laser power can reach 1000 W and the maximum scanning speed is up to 8000 mm/s. The four lasers can work simultaneously. The energy of the laser beam is approximately at the level of Gaussian distribution, and the beam spot diameter is 100 μm. Argon was used as a protection gas and the oxygen content of the forming cabin was controlled below 100 ppm. Multi-laser precision positioning and splicing area precision control technology ensures high-quality, high-efficiency, and high-stability printing. The advanced technology provides technical support for the direct production of large-size, high-precision, and high-performance parts in aerospace, military, and other fields.

2.2. Methods

2.2.1. Process Parameter Optimization

Pore defects are one of the major challenges encountered by SLM. Understanding the relationship between process parameters and pore defects is a prerequisite for producing high-densification parts. The process parameters directly related to pore defects mainly include laser power, scanning speed, hatch spacing, and powder layer thickness [9,39]. In order to obtain the best combination of process parameters, an orthogonal experiment method was employed. Laser power ranged from 140 W to 340 W, scanning speed ranged from 800 mm/s to 1800 mm/s, and hatch spacing ranged from 90 μm to 140 μm. Each parameter included 6 variables. Three factors and six levels were combined into an orthogonal experimental scheme, as shown in Table 2. The powder layer thickness was 30 μm, in accordance with engineering practice.

Table 2. Orthogonal experimental scheme design.

Scheme #	Power /W	Speed /(mm/s)	Hatch /μm	Scheme #	Power /W	Speed /(mm/s)	Hatch /μm
1	140	800	90	19	260	800	120
2	140	1000	100	20	260	1000	130
3	140	1200	110	21	260	1200	140
4	140	1400	120	22	260	1400	90
5	140	1600	130	23	260	1600	100
6	140	1800	140	24	260	1800	110
7	180	800	100	25	300	800	130
8	180	1000	110	26	300	1000	140
9	180	1200	120	27	300	1200	90
10	180	1400	130	28	300	1400	100
11	180	1600	140	29	300	1600	110
12	180	1800	90	30	300	1800	120
13	220	800	110	31	340	800	140
14	220	1000	120	32	340	1000	90
15	220	1200	130	33	340	1200	100
16	220	1400	140	34	340	1400	110
17	220	1600	90	35	340	1600	120
18	220	1800	100	36	340	1800	130

The image method and Archimedes method were used to characterize pore defects. In order to obtain more statistically meaningful data, the sample was designed with a large size of 20 × 20 × 20 mm^3, as shown in Figure 2. After the metal blocks were printed, the surface was burnished to eliminate the interference of sticky powder on the Archimedes test. AG204 analytical balance (Mettler Toledo, Dresden, German) was used to weigh samples with an accuracy of 0.1 mg. The dry weight of the samples was measured before they were immersed in water. Each metal block was measured twice, and the results had to be consistent. The results were recorded as M_{dry}. The metal blocks were weighed again when immersed in water. The measurements were also repeated twice with a deviation controlled within 2.0 mg. The average values were taken and recorded as M_{wet}. The densification is defined by Formula (1). For image characterization, the metal blocks were polished with 180-, 400-, 600-, 800-, 1500-, and 2000-grit sandpapers and 0.05 μm diamond suspension, respectively. Then, an inverted metallographic microscope GX51 (Olympus, Tokyo, Japan) was used to characterize pore defects within the metal blocks.

$$\varphi = \frac{M_{dry}\rho_{water}}{(M_{dry} - M_{wet})\rho_{solid}} \quad (1)$$

ρ_{water} is water density; ρ_{solid} is theoretical density.

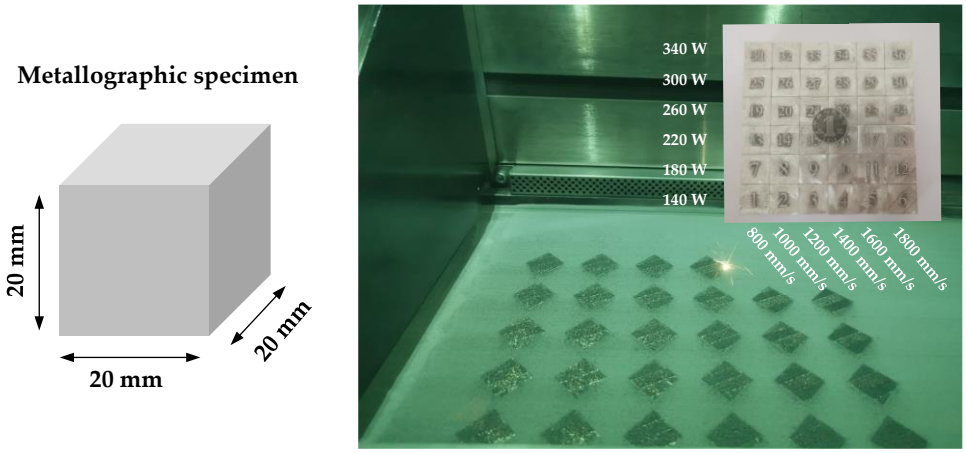

Figure 2. Metallographic block design and printing.

2.2.2. Specimen Design

To investigate the influence of feature size on mechanical properties, corresponding tensile specimens were designed, as shown in Figure 3. The feature size ranged from 0.4 mm to 1.0 mm. Figure 3b illustrates the design of the tensile test rods corresponding to the struts. The building orientation of the tensile test rods coincides with the inclination angle of the struts within the body-centered cube structure, which is 35.3°. Considering that tensile test rods are easily bended by scrapers, support was added to both ends of the rods. Figure 3c illustrates the design of the tensile test piece corresponding to the skin. Tensile test pieces were placed parallel to the building direction. The cross-section of the tensile test piece is rectangular, and the width of the middle section is twice the thickness.

The molten pool width can reach hundreds of microns, which is in the same order of magnitude as feature size, and can easily cause size deviation. In order to realize the high-precision forming of fine structures, BO was used to control size deviation. BO means that the border was offset inward by a certain distance to compensate for size deviation. The molten pool size is determined by the process parameters, meaning that BO should be adjusted according to the specific process scheme. BOs of 0.03 mm, 0.04 mm, 0.05 mm, 0.06 mm, and 0.07 mm were set, respectively, to prepare the specimens. The parameter settings are shown in Table 3. The as-built size was measured and appropriate BOs were matched for different size specimens. Then, tensile specimens were printed in batches. The as-built tensile specimens are shown in Figure 3d,e.

Table 3. BO values for features of different sizes.

Designed Size/mm	BO/mm
0.4, 0.6, 0.8, 1.0	0
0.4, 0.6, 0.8, 1.0	0.03
0.4, 0.6, 0.8, 1.0	0.04
0.4, 0.6, 0.8, 1.0	0.05
0.4, 0.6, 0.8, 1.0	0.06
0.4, 0.6, 0.8, 1.0	0.07

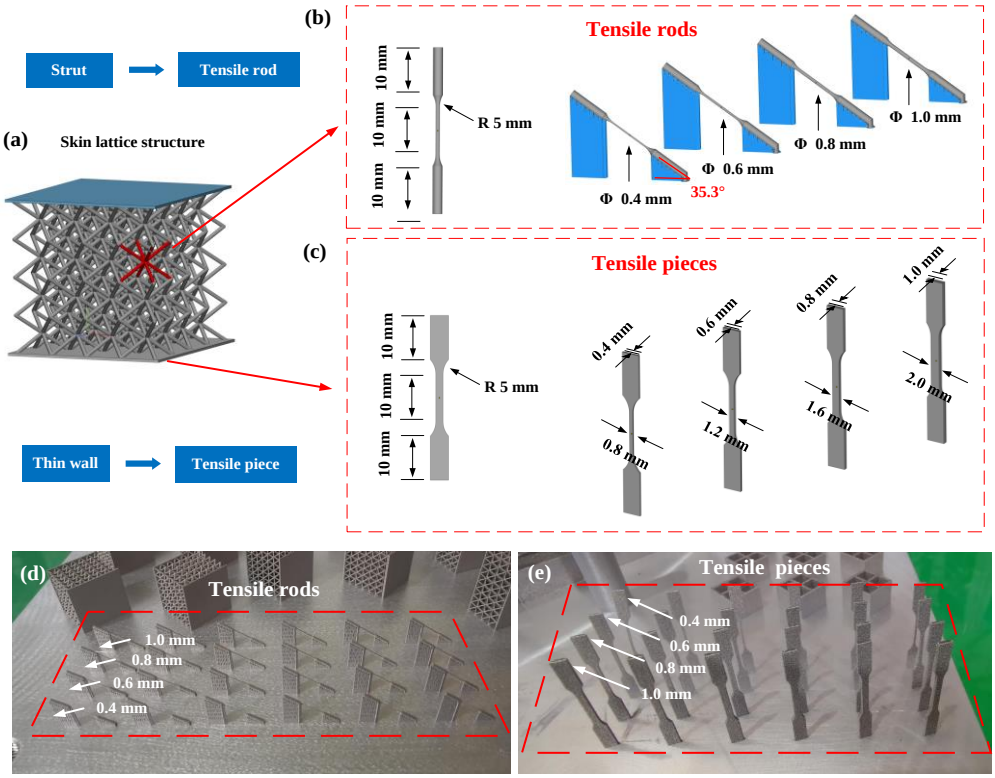

Figure 3. Specimen design for tensile test. (**a**) Skin lattice structure. (**b**) Tensile test rods. (**c**) Tensile test pieces. (**d**) As-built tensile test rods. (**e**) As-built tensile test pieces.

2.2.3. Specimen Characterization

Specimens were annealed at a temperature of 280 °C for 4 h to eliminate residual stress after printing. Ultrasonic cleaning was used to remove the residual powder for about 30 min. An optical microscope Nikon SMZ-745 (Nikon Corporation, Tokyo, Japan) was used to gauge the as-built size under different BOs. A 3D surface profiler ContourGT 3D (Bruker Corporation, Billerica, MA, United States) with a spatial resolution of 1 μm was used to characterize surface morphology, and 300,000 points were collected. Microcomputed tomography YXLON FF35 CT (YXLON International, Hamburg, German) was used to detect pore defects. The scan was performed at 190 kV with a nano-focus ray. When scanned, the sample was rotated at a constant speed of 0.36°/s. The recorded scanning data were imported into VGStudio MAX software (https://www.volumegraphics.com/en/products/vgsm.html, accessed on 25 November 2024) to reconstruct the three-dimensional topographies. All pores larger than 1 μm were within detection range. According to the detected pore size and number, the total volume of pore defects was calculated, and then the porosity of the sample was further defined. The thin walls for microstructure characterization were polished using an argon ion polishing instrument IM4000II (JEOL Ltd., Tokyo, Japan). An electron backscatter diffraction (EBSD) microscope EDAX Velocity Super (EDAX Inc., Pennsylvania, PA, USA) was used to characterize the microstructure.

2.2.4. Tensile Test

Uniaxial tensile testing was carried out at room temperature on a microcomputer-controlled electronic universal testing machine (Lishi LD26.205, Shanghai, China), as shown in Figure 4a. The tensile testing speed was set to 1.0 mm/min. Conventional extensometers and strain gauges are unable to measure the deformation data of submillimeter specimens. Digital image correlation (DIC), a non-contact full-field strain measurement technique, was used to gauge strain. An industrial camera acA2440-35um (Basler, Berlin, German)

was used to record the deformation process of specimens during tensile testing. The camera used a 75 mm telephoto lens. The image acquisition frequency was 2 f/s. A representative stress–strain curve is shown in Figure 4b. Six repeated specimens were tested for each specific size. Elastic modulus, yield strength, ultimate tensile strength, and fracture elongation were calculated based on the tensile stress–strain curve. AlSi10Mg has no obvious yield point, and the stress corresponding to 0.2% strain was taken as the yield strength.

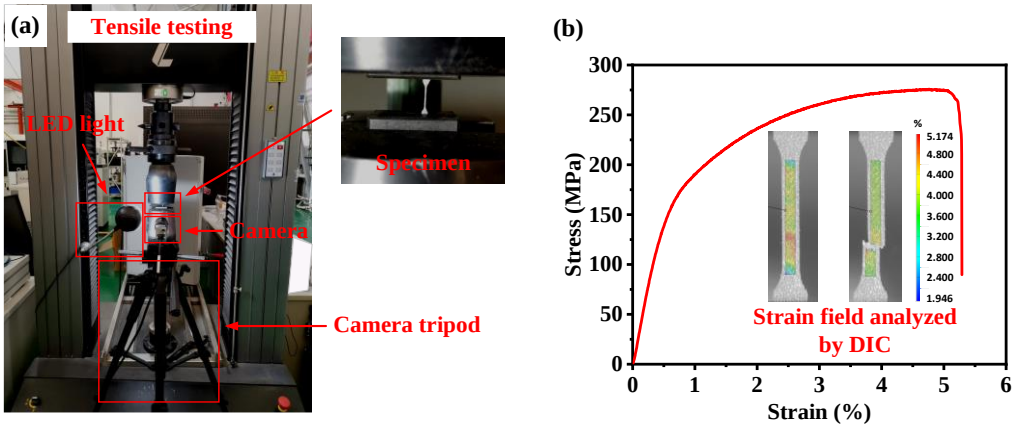

Figure 4. (**a**) Tensile test. (**b**) Stress–strain curve.

3. Results and Discussion

3.1. Optimization of Process Scheme

The internal defects of the metallographic blocks were characterized by optical microscopy. Figure 5 shows the pore defects under different process parameters. Figure 5a–f exhibit the internal pore characteristics with a laser power of 140 W and scanning speed of 800~1800 mm/s. It can be seen that a large number of pores are distributed inside the metallographic blocks. These pores are characterized by irregular shapes, and the size is generally greater than 100 μm. According to these characteristics, the type of the pores can be classified as lack-of-fusion pores. Such defects are mainly caused by insufficient energy input [40]. Increasing the scanning speed from 800 mm/s to 1800 mm/s causes energy density to reduce. As a result, pore size, number, and irregularity significantly increase. At scanning speeds of 1600 mm/s and 1800 mm/s, the pores even interconnect with each other, which is greatly detrimental to the print quality.

When the laser power is increased to 340 W, the number and size of the pores are greatly reduced. The pores are mainly characterized by circular shape. According to the pore morphology, they can be classified as gas pores. Gas pores are mainly caused by trapped gas. When instable flow occurs in a molten pool, the inert gas or gas contained in the raw materials may be involved. If the gas cannot escape before solidification, the residual gas will cause the formation of gas pores. The porosity slightly changes as the scanning speed increases from 800 mm/s to 1800 mm/s. Due to the heterogeneity of pore distribution, the captured images cannot reflect the actual porosity. The Archimedes method was further used to quantify the porosity.

Statistical analysis was performed on the densification of metal blocks treated by different process parameters, and the results are shown in Figure 6. Figure 6a exhibits the densification under different volumetric energy density (E_V). The volumetric energy density is defined by Formula (2) [41,42]. According to the test results, the densification varied from 86.3% to 99.7% under the given process parameters. With the increase in

volumetric energy density, the sample densification showed an increasing trend. When the volumetric energy density exceeded 67 J/mm^3, the densification was almost above 99%.

$$E_v = \frac{P}{v \times l \times h} \tag{2}$$

where P is laser power (W), v is scanning velocity (mm/s), h is the hatch space (mm), and l is the layer thickness (mm).

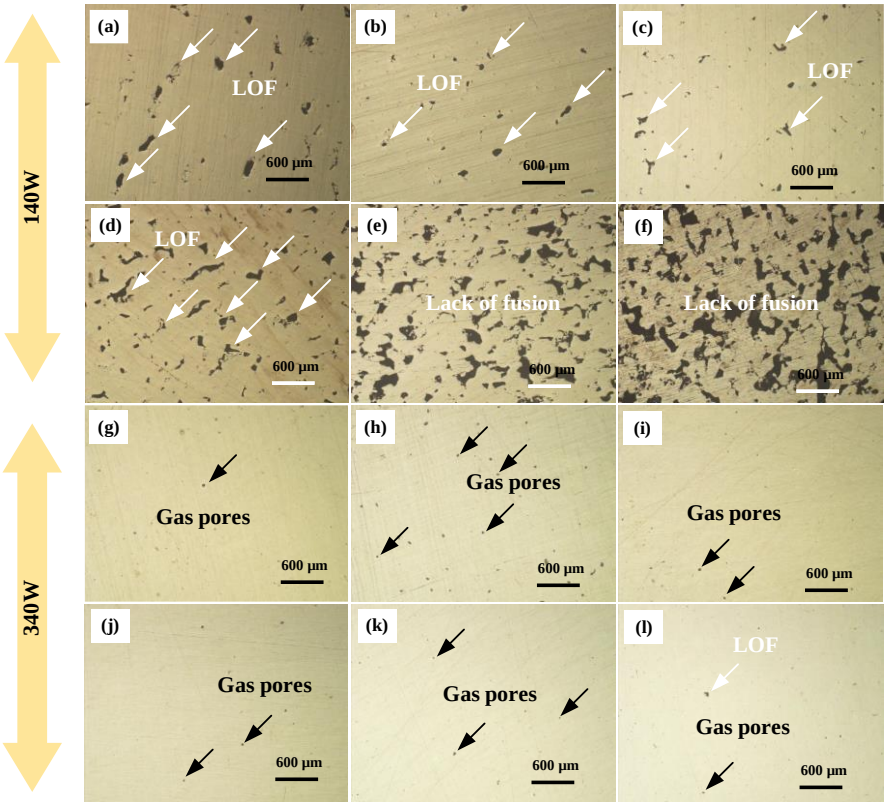

Figure 5. Pore defects of metallographic blocks. (**a**–**f**) Laser power 140 W, scanning speed 800 mm/s, 1000 mm/s, 1200 mm/s, 1400 mm/s, 1600 mm/s, and 1800 mm/s. (**g**–**l**) Laser power 340 W, scanning speed 800 mm/s, 1000 mm/s, 1200 mm/s, 1400 mm/s, 1600 mm/s, and 1800 mm/s.

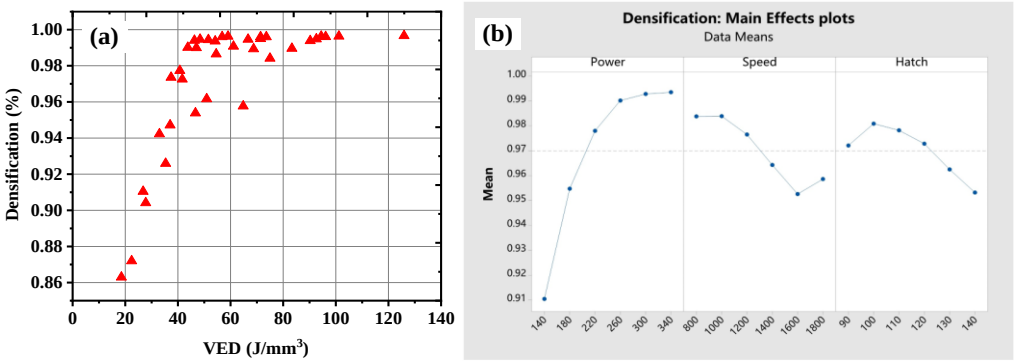

Figure 6. (**a**) Influence of process parameters on porosity. (**b**) Main effects plots for densification.

Minitab statistical software (https://www.minitab.com/en-us/products/minitab/, accessed on 25 November 2024) was used to analyze the influence of laser power, scanning speed, and hatch spacing on densification. Figure 6b exhibits the effect of a single factor on the density. It can be seen that with increases in laser power, the density increases monotonically. Almost full densification could be achieved when the laser power was

340 W. With the increase in scanning speed and hatch spacing, the density decreases. Analysis of variance (ANOVA) was used to further examine the sensitivity of density to these three factors, and the results are shown in Table 4. F-factor is an index for evaluating the sensitivity of the target to the factors. The larger the value, the stronger the influence of this factor. The F-factor of laser power is 28.3, which is much higher than that of the scanning speed and hatch spacing. This phenomenon indicates that laser power is the main factor affecting densification. The F-factor of scanning speed is 4.47, inferior to that of laser power. The F-factor of hatch spacing is the lowest, indicating that the influence on density is the weakest.

Table 4. ANOVA on density.

Source	DF	Seq SS	Contribution	Adj SS	Adj MS	F	P
Power	5	0.031942	70.95%	0.031942	0.006388	28.30	0.000
Speed	5	0.005346	11.87%	0.005346	0.001069	4.74	0.005
Hatch	5	0.003219	7.15%	0.003219	0.000644	2.85	0.042
Error	20	0.004515	10.03%	0.004515	0.000226	-	-
Total	35	0.045021	100.00%	-	-	-	-

The three highest densifications are 99.659%, 99.634%, and 99.629%, respectively, and the corresponding process parameters are listed in Table 5. There is a slight discrepancy among the three values, and the maximum error is only 0.03%. In terms of printing efficiency and energy consumption, these three schemes are significantly different. Scheme 35 has the highest scanning speed and lowest energy density, and the resulting density is slightly smaller than that of the top two schemes. Therefore, considering time and economic cost, scheme 35 is used as the optimized process parameter to prepare the subsequent specimens.

Table 5. The maximum three groups of density corresponding to process parameters.

Scheme #	Power/W	Speed/(mm/s)	Hatch/(μm)	VED/(J/mm^3)	Densification/%
32	340	1000	90	125.9	99.659
31	340	800	140	101.2	99.634
35	340	1600	120	59.0	99.629

3.2. Effect of Feature Size on Dimensional Accuracy

The actual size of 0.4~1.0 mm cylindrical struts under different BOs was measured, and the data are depicted in Figure 7. When BO is 0 mm, the actual size of all specimens is larger than the designed size. This is because the BO of 0 mm implies that the scanning tracks are filled directly within the geometry border, and the molten pool will cross the border, causing the actual size to exceed the designed size. The size deviation for the 0.4 mm strut is 0.075 mm, and the relative error is 18.75%. When the diameter increases to 1.0 mm, the dimensional error reaches 0.161 mm, and the relative error is 16.15%. The increase in designed size causes an increasing trend of absolute size error. In contrast, the relative size error is relatively stable, fluctuating in the range of 15% to 20%.

The influence mechanism of the diameter of the strut on the absolute size error can be attributed to the heat accumulation during the forming process. Heat accumulation occurs when the heat dissipation efficiency is lower than the heat input efficiency, which causes the temperature to rise. The high-energy laser beam is the main source of heat input. As the top-layer material is heated by the laser beam, the heat energy, on the one hand, will be conducted downward to the substrate, and on the other hand, will be transferred to the surrounding powder by the lateral surface, as illustrated by Figure 8a,b. The thicker strut

possesses a smaller specific surface area compared with the thinner strut, which reduces the heat dissipation efficiency of the lateral surface. In addition, the larger cross-section area of the thicker strut means that the laser provides more energy on the top layer. Therefore, there is stronger heat accumulation on the thicker strut. Regarding the influence of size on macroscopic heat accumulation, Patcharapit Promoppatum [36] conducted a detailed study.

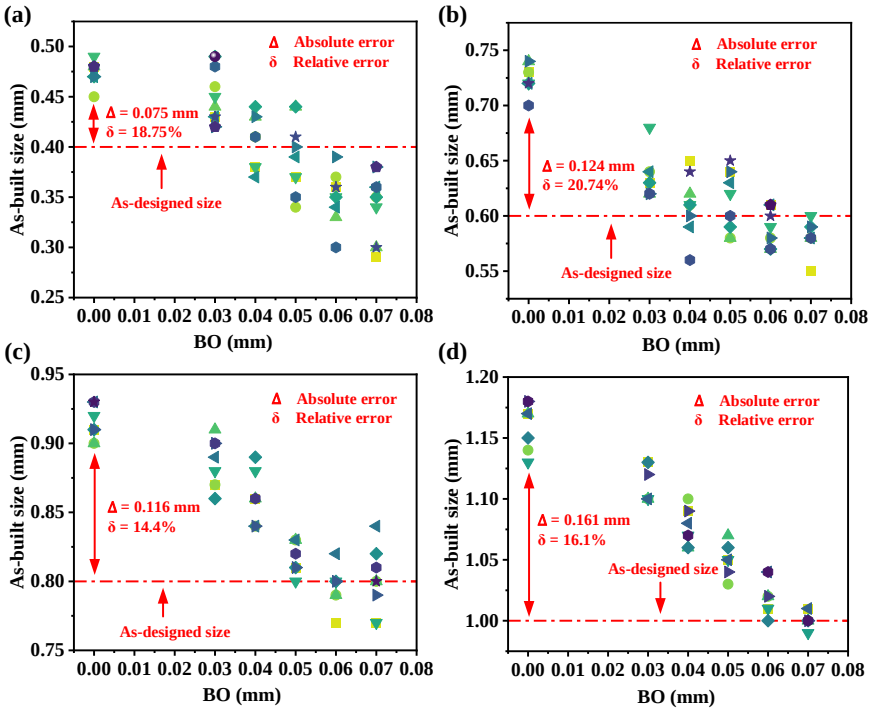

Figure 7. The actual size of the cylindrical strut: (**a**) 0.4 mm, (**b**) 0.6 mm, (**c**) 0.8 mm, (**d**) 1.0 mm.

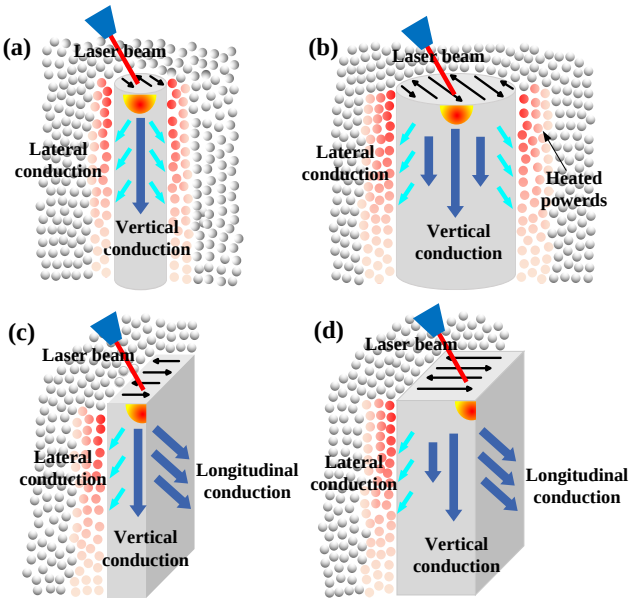

Figure 8. Schematic diagram of heat transfer in struts and thin walls of different sizes during the forming process: (**a**) thinner strut, (**b**) thicker strut, (**c**) thinner wall, (**d**) thicker wall.

Affected by heat accumulation, the temperature on the top layer of the larger strut is higher and causes more powder near the border to melt, resulting in a larger size error. To improve the forming accuracy, an appropriate BO was matched for the struts. It can be found that with the increase in BO, the actual size gradually decreases and approaches

the designed size. The statistical data are listed in Table 6. When BO was set to 0.04 mm, 0.06 mm, 0.06 mm, and 0.07 mm, respectively, the as-built size of the struts with diameters of 0.4 mm, 0.6 mm, 0.8 mm, and 1.0 mm could reach a good agreement with the designed size.

Table 6. Statistical table of as-built size under different BOs.

Sample	BO/mm	0.4 mm	0.6 mm	0.8 mm	1.0 mm
Struts	0	0.48 ± 0.0108	0.72 ± 0.01236	0.92 ± 0.01236	1.16 ± 0.01885
	0.03	0.45 ± 0.027	0.64 ± 0.02	0.89 ± 0.01773	1.11 ± 0.01464
	0.04	0.41 ± 0.02669	0.61 ± 0.02646	0.86 ± 0.01885	1.08 ± 0.01488
	0.05	0.39 ± 0.03606	0.61 ± 0.02744	0.82 ± 0.01165	1.05 ± 0.01291
	0.06	0.35 ± 0.0255	0.59 ± 0.01729	0.80 ± 0.01512	1.02 ± 0.01414
	0.07	0.34 ± 0.03315	0.58 ± 0.01458	0.80 ± 0.02236	1.00 ± 0.00641
Thin walls	0	0.59 ± 0.01986	0.80 ± 0.01667	1.00 ± 0.01885	1.18 ± 0.01246
	0.03	0.51 ± 0.02698	0.73 ± 0.02121	0.92 ± 0.0207	1.17 ± 0.03159
	0.04	0.51 ± 0.03105	0.69 ± 0.03739	0.89 ± 0.01996	1.08 ± 0.01915
	0.05	0.48 ± 0.01959	0.67 ± 0.0239	0.87 ± 0.01773	1.06 ± 0.01642
	0.06	0.42 ± 0.01093	0.63 ± 0.01922	0.83 ± 0.01246	1.03 ± 0.02031
	0.07	0.39 ± 0.02728	0.59 ± 0.02242	0.81 ± 0.02295	1.01 ± 0.02167

Figure 9 depicts the as-built size of 0.4~1.0 mm thin walls under different BOs. When the BO is 0 mm, the actual size is greater than the designed size, with deviation ranging from 0.18 mm to 0.21 mm. The size deviation is relatively stable and does not show dependence on wall thickness. The schematic diagram of the heat transfer of the thin-wall structure during the forming process is illustrated in Figure 8c,d. Compared to the heat transfer of the cylindrical strut, except for the lateral heat dissipation and downward heat conduction, the length direction of the thin wall also provides space for heat transfer, resulting in no obvious difference in heat accumulation for different wall thickness structures. In addition, there are more scanning tracks on the thin-wall structure; in other words, more energy will be input on the top layer, promoting heat accumulation and causing the dimensional errors to exceed 0.18 mm.

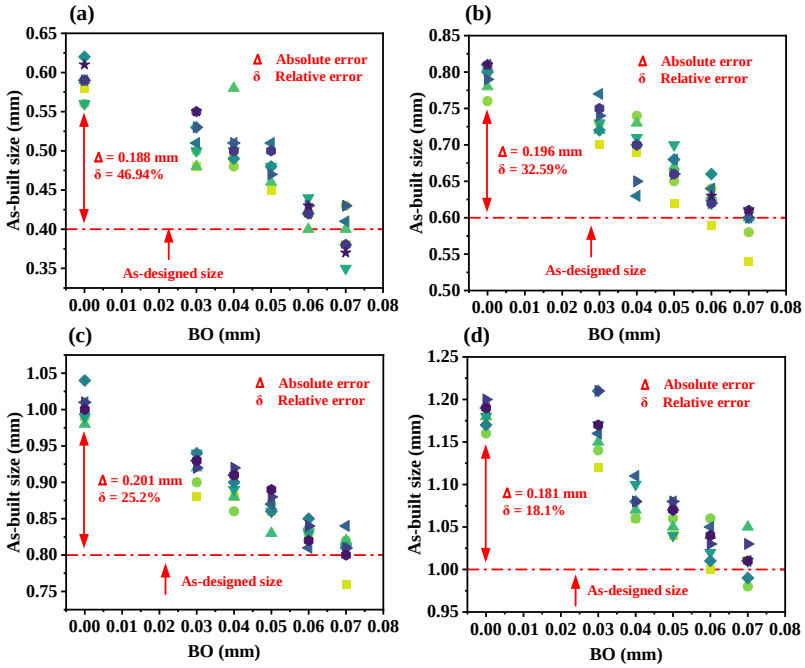

Figure 9. The actual size of the thin wall: (**a**) 0.4 mm, (**b**) 0.6 mm, (**c**) 0.8 mm, (**d**) 1.0 mm.

The relative size error for the 0.4 mm thin-wall structure is the largest, at close to 50%. When the designed size increases to 1.0 mm, the relative size error is reduced to less than 20%. This indicates that the size control for the thin-wall structure with submillimeter thickness needs to be paid more attention. In order to achieve high-precision forming, it is necessary to match an appropriate BO for thin-wall structures with different thicknesses. According to the statistical results in Table 6, when BO is set to 0.07 mm, all thin-wall structures can be printed precisely.

3.3. Effect of Feature Size on Roughness

A 3D surface profiler was used to characterize the surface topography of the thin-wall specimens. Figure 10a–d show the surface topography characteristics of the thin walls with a thickness of 0.4~1.0 mm. The surfaces of the thin walls are rough and uneven, and the roughness is almost in the range of 0~100 μm. Surface quality is mainly determined by two factors. One factor is adhesive powders. Partially melted powder—firmly adhered to the surface and difficult to remove by ultrasonic cleaning—is the main contributor to surface roughness. Another one is the irregularity of the solidified molten pools. The semi-ellipsoidal morphology of the molten pools and overlap at the model boundary cause the formation of an uneven surface, as shown in Figure 10e. The deflection of scanning tracks between successive layers is usually used to control the thermal stress during the printing process, but the deflection of scanning direction will lead to different ditch on the surface and affect the surface quality.

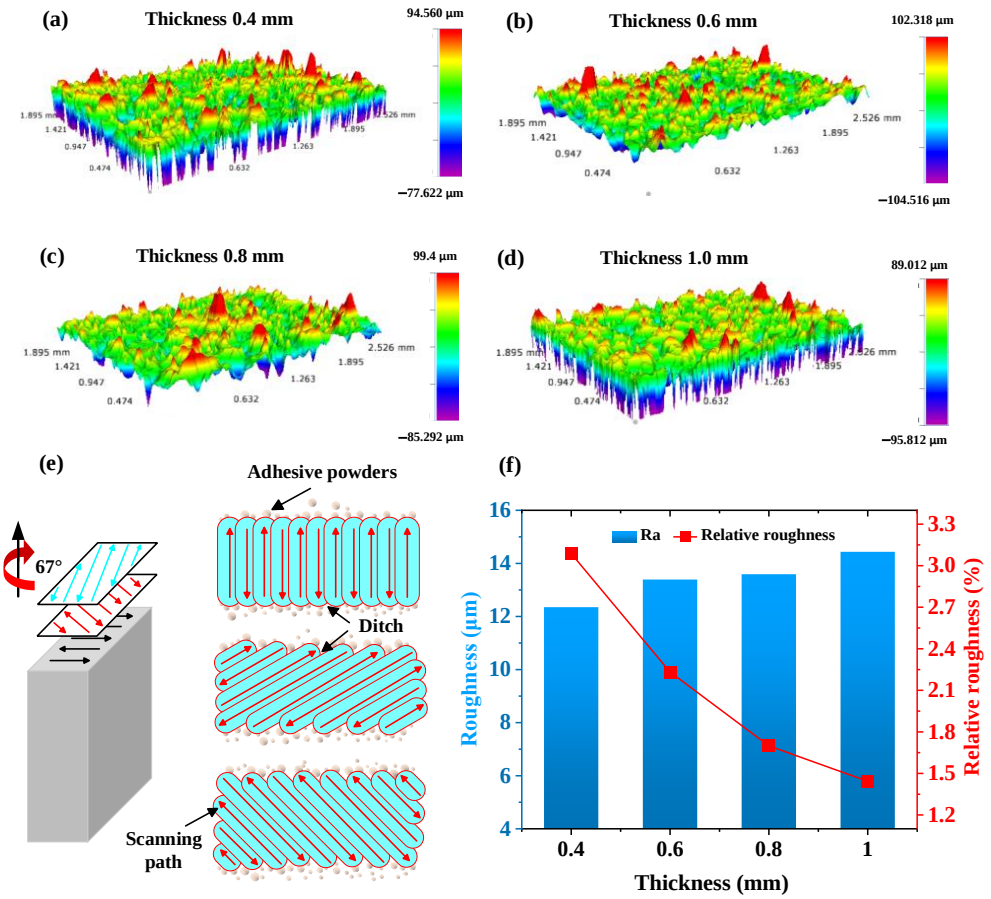

Figure 10. Three-dimensional surface topography of thin-wall structure: (**a**) 0.4 mm, (**b**) 0.6 mm, (**c**) 0.8 mm, (**d**) 1.0 mm, (**e**) schematic diagram of rough surface by SLM, (**f**) relation of roughness with thickness.

The surface roughness of thin-walled structures was statistically analyzed, and the results are shown in Figure 10f. The absolute roughness varies in the range of 12~14 μm, and increases gently with the increase in wall thickness. The variation in roughness can be attributed to the influence of wall thickness on temperature field. The 0.4 mm thin-walled structure is relatively narrow and reduces the heat conduction efficiency. More heat energy is transferred through the lateral surface to the surrounding powder, as shown in Figure 8c. As a result, the powder near the wall surface can be melted more fully. The 1.0 mm thin-wall structure has a larger space for heat conduction, and can conduct heat to the substrate more efficiently, as shown in Figure 8d. In this case, less heat is dissipated through the wall surface, resulting in the powder near the surface being melted incompletely and adhering to the wall surface, increasing the roughness. However, the relative roughness of the 0.4 mm thin-wall structure is more than 3%, while the relative roughness of the 1.0 mm thin-wall structure is less than 1.5%. The relative roughness decreases significantly with the increase in wall thickness.

3.4. Effect of Feature Size on Porosity

The internal pore defects of the struts were evaluated based on the 3D reconstruction model. Figure 11. demonstrates the pore morphology and size distribution within the struts with a diameter of 0.4~1.0 mm. The porosity is below 1% for all struts, which means the optimized process parameters based on large-size metal blocks are also suitable for the manufacturing of fine structures. Figure 12. shows that with the increase in diameter, the porosity declines. When the diameter increases from 0.4 mm to 1.0 mm, the porosity declines from 0.696% to 0.032%. Regarding the influence of feature size on porosity, Dong et al. [30] drew the same conclusion. Meanwhile, it is noted that under the same conditions, the struts in the present study have a lower porosity. This proves the superiority of the optimized process parameters in this work.

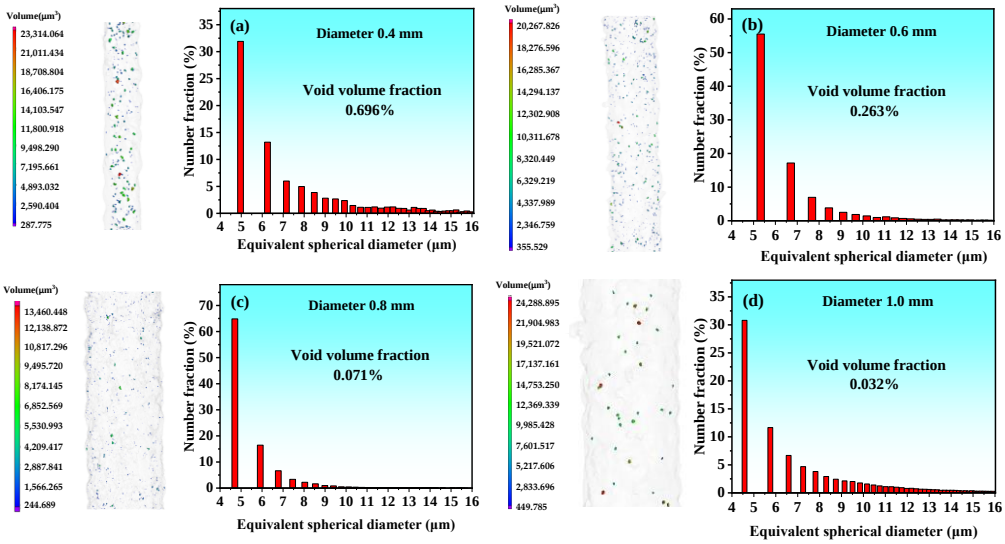

Figure 11. Morphology and size distribution of the pore defects within the struts: (**a**) 0.4 mm, (**b**) 0.6 mm, (**c**) 0.8 mm, (**d**) 1.0 mm.

The pores within struts are dominated by circular pores, which are usually caused by residual gas in the molten pool [43]. Gas pores are mainly caused by an unstable flow in the molten pool. Influenced by recoil pressure, protective gas is easily involved in the molten pool. If these gases do not escape before the solidification of the molten pool, they will be captured and form pores. The influence mechanism of the strut diameter on porosity lies in its influence on the temperature field. The space for heat conduction in the 0.4 mm strut is

small, limiting the efficiency of heat dissipation. In addition, the small cross-sectional area of the 0.4 mm strut means that the scanning tracks on the top layer are short, shortening the scanning time for single tracks. Before the molten pool on the current track solidifies completely, the laser beam begins to scan along the next track. Under this circumstance, continuous heat input easily causes unstable flow in the molten pool, introducing pore defects. The 1.0 mm strut has a larger cross-section area, providing a larger space for heat dissipation. Also, longer scanning tracks allow more time for heat dissipation. Therefore, the duration of the molten pool is short, which can suppress the unstable flow of the molten pool, reducing pore defects. According to previous reports, some scholars found [44,45] that unstable energy input in the laser turn point or stopping emitting light at the end of tracks could also cause pore defects.

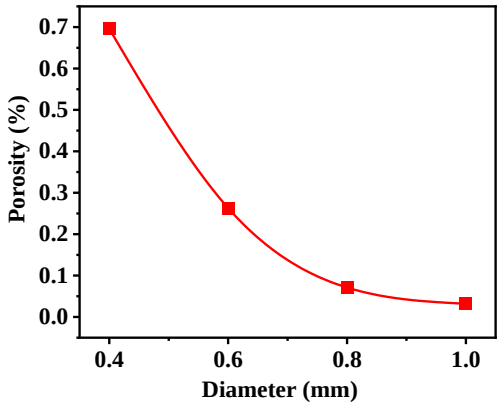

Figure 12. Porosity of struts with different diameters.

3.5. Effect of Feature Size on Microstructure

The longitudinal sections (XZ plane) of the thin-walled structures were examined, and the microstructure was characterized by EBSD. The inverse pole figures (IPFs) and grain statistics information are shown in Figure 13. The EBSD maps show that the α-Al matrix is mainly composed of elongated columnar grains and fine equiaxial grains. The morphology of the molten pool can be distinguished by the distribution of crystals. Affected by the heat flow direction, the grains within the molten pool grew epitaxial towards the center and formed columnar crystals. At the edge of the molten pool, the cooling rate was higher. The grains did not develop fully and formed fine equiaxed crystals.

The average grain sizes of the 0.4~1.0 mm thin walls are plotted in Figure 13e. As the thickness increased from 0.4 mm to 0.8 mm, the grain size increased from 11.6 μm to 12.7 μm. When the thickness further increased to 1.0 mm, the grain size reduced to 12.0 μm. The analysis shows that the heat transfer condition, determined by wall thickness, is responsible for the variation in grain size. High-efficiency heat transfer implies a high cooling rate that is more prone to generate fine grains. The thinner structures possess higher specific surface area, which is beneficial for heat transferring through the surface. With thickness increasing, heat conduction gradually becomes the main mode of heat dissipation. The two modes of heat transfer are competitive. In thin walls with a thickness less than 0.8 mm, heat is mainly transferred through the surface. The increase in thickness accompanied with the decrease in specific surface area, weakening the heat transfer efficiency, led to an increase in grain size. When the wall thickness exceeds 0.8 mm, heat is mainly transferred through the as-deposited entity, which can effectively improve the heat sinking efficiency and result in a decrease in grain size.

Figure 13f shows the variation in the grain aspect ratio with wall thickness. A high aspect ratio indicates that the grains are elongated to a great extent. With the increase in wall thickness, the aspect ratio decreased first and then increased, varying in the range of

2.74~3.14. The aspect ratio showed no significant correlation with wall thickness. Figure 13g displays the relationship between grain orientation and wall thickness. With the increase in thickness, the grain arrangement is more inclined in the built direction, indicating the heat flow direction gradually converts from the lateral side to the downward direction.

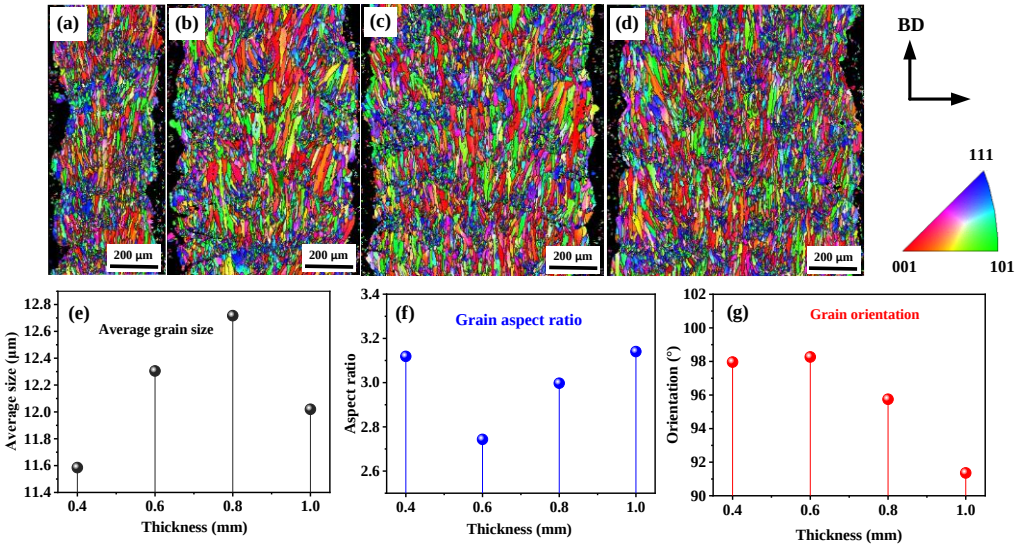

Figure 13. Microstructure characteristics: (**a**–**d**) EBSD inverse pole figure orientation maps for thin walls with thickness of 0.4~1.0 mm, (**e**) grain size, (**f**) aspect ratio, (**g**) grain orientation.

3.6. Mechanical Properties Before Polishing

Tensile tests were performed at room temperature to investigate the effects of defects and microstructure on the mechanical properties. Figure 14. exhibits the stress–strain curves of the tensile specimens with a size of 0.4~1.0 mm. Figure 14a and b correspond to the stress–strain curves of the tensile test rods and tensile test pieces, respectively. As can be seen from the figure, there are slight differences in the stress–strain curves between tensile test specimens with the same size. This phenomenon can be attributed to random defects introduced during the printing process, such as microscopic pores and cross-section size variation. Comparing the stress–strain curves of the specimens of different sizes, there are obvious differences in elongation to fracture. For the tensile test piece, the thickness not only affects the elongation, but also has an obvious influence on the ultimate tensile strength.

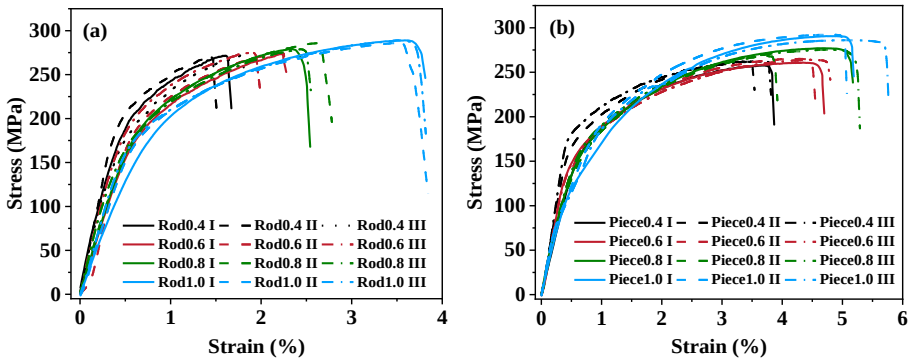

Figure 14. Stress–strain curve for tensile specimen: (**a**) tensile test rod, (**b**) tensile test piece.

Based on the stress–strain curves, mechanical properties such as elastic modulus, yield strength, ultimate tensile strength, and fracture elongation were statistically analyzed, and the results are shown in Figure 15. Figure 15a compares the Young's modulus of the tensile test rods and the tensile test pieces. The Young's modulus of the tensile test rods is in

the range of 34.3~51.3 GPa, which is similar to the values reported by Dong et al. [46]. In terms of the tensile test pieces, the Young's modulus varies in the range of 58.1~71.5 GPa. The variation trend of the elastic modulus does not show a correlation with geometry size. Figure 15b compares the yield strength of the tensile test specimens of different sizes. The yield strength of the tensile test rods and pieces varies in the range of 194.0~215.1 MPa and 167.6~181.3 MPa, respectively. The statistical result also does not show the dependency of yield strength on geometry size.

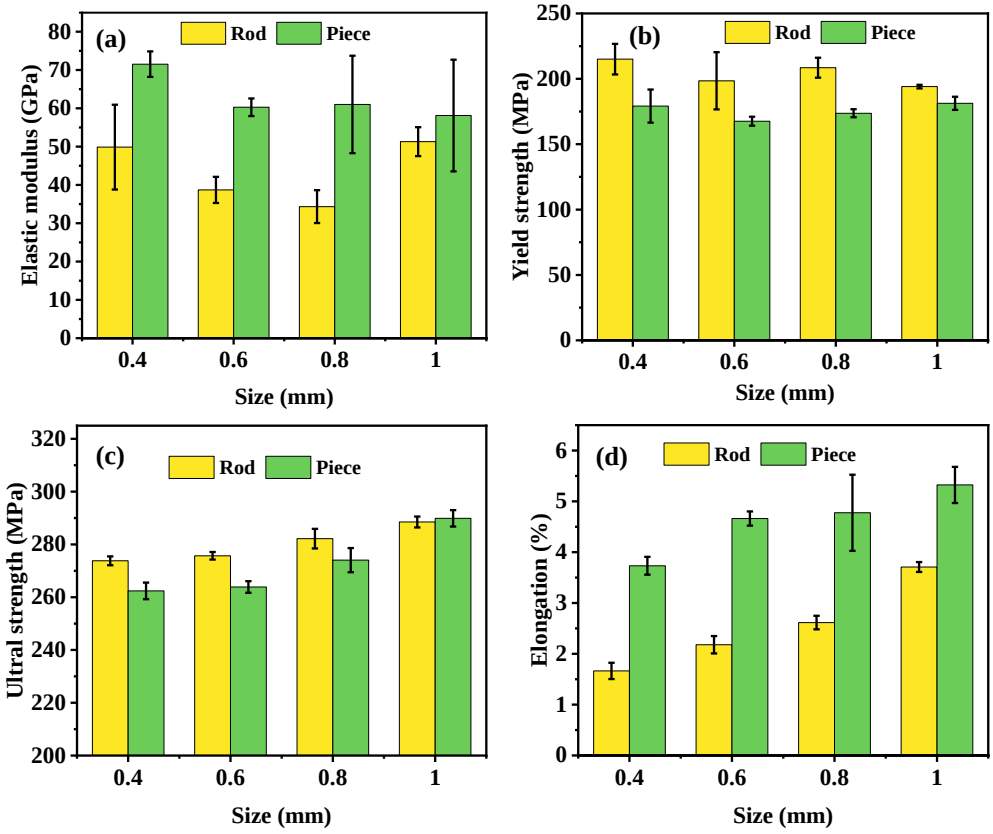

Figure 15. Mechanical properties of tensile test rods and pieces: (**a**) elastic modulus, (**b**) yield strength, (**c**) ultimate strength, (**d**) elongation.

In contrast to the elastic modulus and yield strength, ultimate tensile strength has an obvious correlation with geometry size, as illustrated in Figure 15c. With the increase in thickness, the tensile strength shows an increasing trend. With increasing specimen size from 0.4 mm to 1.0 mm, the tensile strength of the test rods increases from 273.8 MPa to 288.5 MPa, with an increment of about 15 MPa. The tensile strength of the test piece increases from 262.4 MPa to 289.9 MPa; the increase is 37.5 MPa. Figure 15d compares the fracture elongation of the tensile specimens of different sizes. With the increase in size, the elongation is obviously enhanced. The elongation of the test rod with a diameter of 0.4 mm is 1.66%. When the diameter increases to 1.0 mm, the elongation rises to 3.7%, and the increase exceeds one time. The fracture elongation of the 0.4 mm tensile test piece is 3.7%. When the thickness increases to 1.0 mm, the elongation rises to 5.3%.

The analysis shows that surface quality and internal pore defects are the key factors affecting tensile strength and elongation. Figure 16a–d show the optical image of the longitudinal section of the thin-walled structure and the corresponding contour lines. A random distribution of microscopic pores can be observed in the longitudinal section. Influenced by SLM's layer-by-layer forming characteristics, irregular bumps and dents are distributed along the vertical border of the longitudinal section. Figure 16e demonstrates

the influence mechanism of the surface defects and internal pores on mechanical properties. When tensile load is applied, these dents and pores will become the stress concentration point, leading to the initiation of the propagation of cracks, reducing the strength and ductility. Specimens of different sizes possess different specific surface areas. Figure 16f compares the specific surface areas of specimens of different sizes. For the cross-section of the tensile test piece, the width is two times the thickness. With the increase in wall thickness, the specific surface area decreases rapidly. This means that the influence of surface quality on the mechanical properties is gradually reduced. Therefore, with the increase in wall thickness, the tensile strength and fracture elongation of the test piece both show an increasing trend.

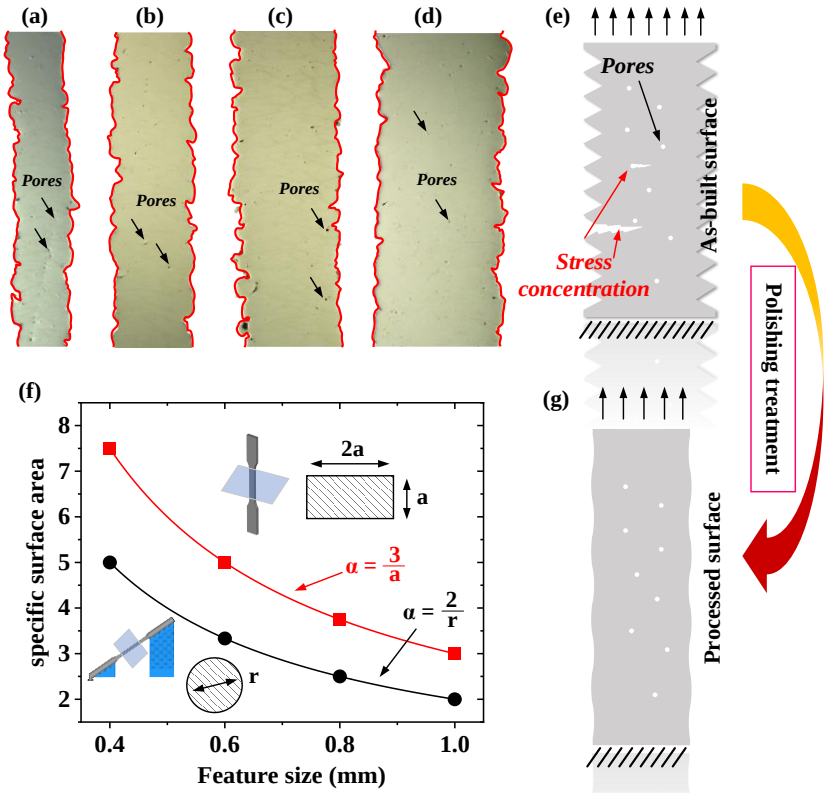

Figure 16. (**a**–**d**) OM images of surface morphology of 0.4~1.0 mm thin walls; (**e**) schematic diagram of influence mechanism of defects on mechanical properties; (**f**) specific surface of tensile test rods and pieces of different sizes; (**g**) schematic diagram of polished surface.

The increase in the tensile test rod diameter leads to a decrease in the specific surface area, which makes the large-size tensile test rod exhibit better mechanical properties. It is noted that the specific surface area of the tensile test piece is higher than that of the tensile test rod with the same size, but the fracture elongation is higher for the tensile test piece. The reason for this may be attributed to the build orientation. Different orientations produce different microstructures, which may affect the fracture elongation.

3.7. Mechanical Properties After Polishing

The tensile test pieces were polished with 240-grit sandpaper, and the bilateral polishing thickness was 0.05 mm~0.2 mm. The surface topography before and after polishing is shown in Figure 17a. The polishing treatment effectively reduced the surface roughness from 13.6 μm to 0.56 μm. Tensile test was performed on the polished specimen, and the stress–strain curves are shown in Figure 18b. To avoid the figure being polluted by numerous data, only a representative curve is displayed for the same size specimens. From

the figure, we can see that significant improvements in ultimate strength and ductility are realized after the polishing treatment.

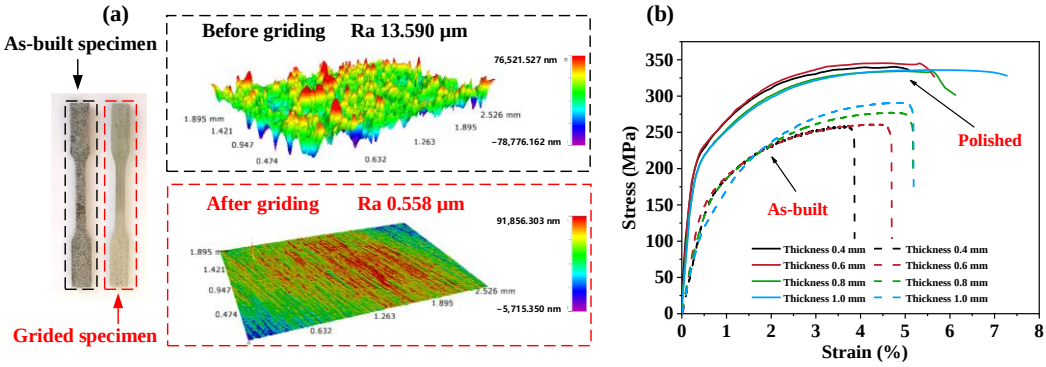

Figure 17. (**a**) Surface morphology before and after polishing; (**b**) tensile stress–strain curves before and after polishing.

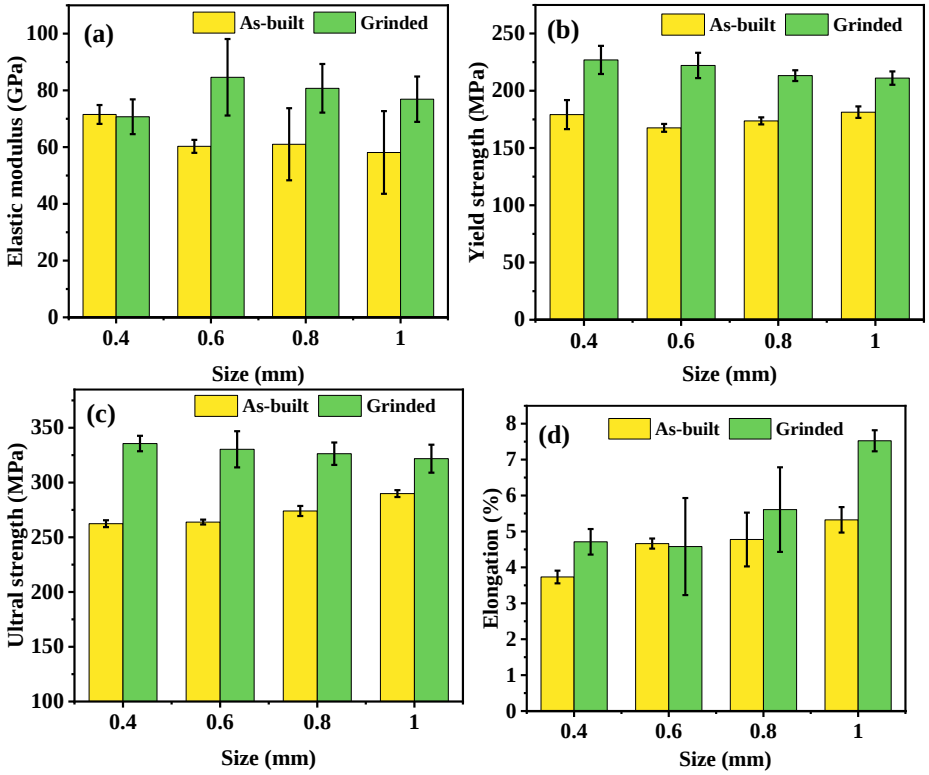

Figure 18. Comparison of mechanical properties of the test piece before and after polishing: (**a**) elastic modulus, (**b**) yield strength, (**c**) ultimate strength, (**d**) elongation.

Young's modulus, yield strength, ultimate tensile strength, and elongation were calculated based on the stress–strain curves, and the results are shown in Figure 18. Through comparison, it is found that the mechanical properties of the tensile specimens are improved by the polishing treatment to different extents. The elastic modulus of all tensile specimens after polishing exceeds 70 GPa. For the specimen with a wall thickness of 0.6~1.0 mm, the elastic modulus was significantly increased by about 20 GPa. The yield strength of the polished specimens is in the range of 211.1~226.9 MPa, which is higher than that of the untreated specimens at 167.6~181.3 MPa. In terms of tensile strength, the polishing treatment makes the tensile strength of the test pieces exceed 320 MPa, reaching the level of casting, and the increase is more than 30 MPa. At the same time, it is noted that increase in the yield strength and tensile strength of the 0.4 mm thin wall after polishing are

significantly higher than the amplitude corresponding to the 1.0 mm thin wall, indicating that the polishing treatment is more effective for small-feature structures. In terms of elongation, the thin walls of 0.4, 0.8, and 1.0 mm show better ductility after polishing, while the elongation of the thin wall of 0.6 mm does not improve significantly. Experimental error may be responsible for this phenomenon.

Comprehensive analysis shows that polishing treatments can significantly improve the mechanical properties of fine features. The mechanism behind this lies in the improvement of surface quality. Figure 16e,g show the schematic diagram of the surface morphology before and after polishing. Without the polishing treatment, there are vulnerable points on the surface that may cause stress concentration, which can easily lead to crack initiation. After the polishing treatment, these sharp concaves are smoothed and there are few vulnerable points near the surface, resulting in better mechanical properties. This analysis shows that surface quality is a key factor affecting the mechanical properties, and the improvement of surface quality can be an effective way to enhance the mechanical properties of structures. This also implies that polishing post-treatment can realize further weight reduction for lightweight structures.

4. Conclusions

In the present work, the features of skin lattice structures, such as struts and thin walls, were taken as samples to investigate the effect of geometry size on dimension accuracy, pore defects, roughness, and microstructure. Through tensile tests, the relationship between feature size and mechanical properties was investigated. A polishing treatment was implemented to explore the improvement to mechanical properties. The following conclusions are drawn based on this study:

1. Submillimeter features fabricated using optimized process parameters can reach a densification of above 99%, demonstrating that optimized process parameters based on large size samples (20 mm) are also applicable for the formation of submillimeter features.
2. When the diameter of a strut increases from 0.4 mm to 1.0 mm, the size error increases from 0.075 mm to 0.161 mm. The dimensional error for thin-walled structures is relatively stable. The difference in heat accumulation is responsible for dimensional errors. When matched with a suitable BO, all features of different sizes can be printed precisely.
3. When the thickness is increased from 0.4 mm to 1.0 mm, the porosity is reduced from 0.7% to 0.03%, and the relative roughness is reduced from 3.1% to 1.4%. After being processed with polishing treatment, roughness can be reduced to below 0.5 μm. The grain size and aspect ratio do not show a dependence on specimen size.
4. Increasing feature size will reduce the specific surface area and weaken the negative impact of the rough surface on mechanical properties, so large-size specimens show higher tensile strength and elongation. Elastic modulus and yield strength have no obvious correlation with feature size. Polishing treatments are an effective way to improve surface quality. By diminishing the points of stress concentration near the surface, the mechanical properties of fine features can be remarkably enhanced.

Author Contributions: Conceptualization, J.Q., R.T. and W.L.; Methodology, C.P., S.Y. and R.T.; Software, C.P. and W.L.; Validation, S.Y. and H.S.; Formal analysis, C.P. and S.Z.; Investigation, C.P.; Resources, J.Q.; Data curation, C.P. and R.T.; Writing—original draft preparation, C.P.; Writing—review and editing, C.P.; Visualization, C.P.; Supervision, H.S., S.Z. and R.T.; Project administration, J.Q.; Funding acquisition, J.Q. All authors have read and agreed to the published version of the manuscript.

Funding: We are grateful for the financial support provided by the 'National Key Research and Development Program of China' (2023YFB4605600), the 'Research Project of National Civil Aerospace (D020302), and the 'Multi-laser powder bed additive manufacturing technology and equipment' (2023YFB4604900).

Data Availability Statement: The authors declare that the data supporting the findings of this work are available within the paper. Should any raw data files be needed in another format, they are available from the corresponding author upon reasonable request.

Conflicts of Interest: Authors Chengkuan Peng, Junfeng Qi, Sanqiang Yang, Heng Shao and Weining Li were employed by the company Beijing Spacecraft Manufacturing Co. The remaining authors declare that the research was conducted in the absence of any commercial or financial relationships that could be construed as a potential conflict of interest.

References

1. Du Plessis, A.; Razavi, N.; Benedetti, M.; Murchio, S.; Leary, M.; Watson, M.; Bhate, D.; Berto, F. Properties and applications of additively manufactured metallic cellular materials: A review. *Prog. Mater. Sci.* **2022**, *125*, 100918. [CrossRef]
2. Xu, P.; Lan, X.; Zeng, C.; Zhang, X.; Zhao, H.; Leng, J.; Liu, Y. Compression behavior of 4D printed metamaterials with various Poisson's ratios. *Int. J. Mech. Sci.* **2024**, *264*, 108819. [CrossRef]
3. Jiang, W.; Yin, G.; Xie, L.; Yin, M. Multifunctional 3D lattice metamaterials for vibration mitigation and energy absorption. *Int. J. Mech. Sci.* **2022**, *233*, 107678. [CrossRef]
4. You, J.H.; Park, K. Design and additive manufacturing of thermal metamaterial with high thermal resistance and cooling capability. *Addit. Manuf.* **2021**, *41*, 101947. [CrossRef]
5. Jiang, W.; Yan, L.; Ma, H.; Fan, Y.; Wang, J.; Feng, M.; Qu, S. Electromagnetic wave absorption and compressive behavior of a three-dimensional metamaterial absorber based on 3D printed honeycomb. *Sci. Rep.* **2018**, *8*, 4817. [CrossRef]
6. Wu, L.; Zhai, Z.; Zhao, X.; Tian, X.; Li, D.; Wang, Q.; Jiang, H. Modular Design for Acoustic Metamaterials: Low-Frequency Noise Attenuation. *Adv. Funct. Mater.* **2022**, *32*, 2105712. [CrossRef]
7. Liu, Y.; Tan, Q.; Lin, H.; Wang, J.; Wang, K.; Peng, Y.; Yao, S. Integrated design and additive manufacturing of lattice-filled multi-cell tubes. *Compos. Sci. Technol.* **2023**, *243*, 110252. [CrossRef]
8. Sun, Q.; Zhi, G.; Zhou, S.; Tao, R.; Qi, J. Compressive Mechanical and Heat Conduction Properties of AlSi10Mg Gradient Metamaterials Fabricated via Laser Powder Bed Fusion. *Chin. J. Mech. Eng.* **2024**, *37*, 123. [CrossRef]
9. Limbasiya, N.; Jain, A.; Soni, H.; Wankhede, V.; Krolczyk, G.; Sahlot, P. A comprehensive review on the effect of process parameters and post-process treatments on microstructure and mechanical properties of selective laser melting of AlSi10Mg. *J. Mater. Res. Technol.* **2022**, *21*, 1141–1176. [CrossRef]
10. Wu, L.; Xue, J.; Tian, X.; Liu, T.; Li, D. 3D-printed Metamaterials with Versatile Functionalities. *Chin. J. Mech. Eng. Addit. Manuf. Front.* **2023**, *2*, 100091. [CrossRef]
11. Dzugan, J.; Seifi, M.; Prochazka, R.; Rund, M.; Podany, P.; Konopik, P.; Lewandowski, J.J. Effects of thickness and orientation on the small scale fracture behaviour of additively manufactured Ti-6Al-4V. *Mater. Charact.* **2018**, *143*, 94–109. [CrossRef]
12. Liu, L.Y.; Yang, Q.S.; Zhang, Y.X. Plastic damage of additive manufactured aluminium with void defects. *Mech. Res. Commun.* **2019**, *95*, 45–51. [CrossRef]
13. Wei, P.; Wei, Z.; Chen, Z.; Du, J.; He, Y.; Li, J.; Zhou, Y. The AlSi10Mg samples produced by selective laser melting: Single track, densification, microstructure and mechanical behavior. *Appl. Surf. Sci.* **2017**, *408*, 38–50. [CrossRef]
14. Chen, B.; Yao, Y.; Song, X.; Tan, C.; Cao, L.; Feng, J. Microstructure and mechanical properties of additive manufacturing AlSi10Mg alloy using direct metal deposition. *Ferroelectrics* **2018**, *523*, 153–166. [CrossRef]
15. Poncelet, O.; Marteleur, M.; van der Rest, C.; Rigo, O.; Adrien, J.; Dancette, S.; Jacques, P.J.; Simar, A. Critical assessment of the impact of process parameters on vertical roughness and hardness of thin walls of AlSi10Mg processed by laser powder bed fusion. *Addit. Manuf.* **2021**, *38*, 101801. [CrossRef]
16. Roach, A.M.; White, B.C.; Garland, A.; Jared, B.H.; Carroll, J.D.; Boyce, B.L. Size-dependent stochastic tensile properties in additively manufactured 316L stainless steel. *Addit. Manuf.* **2020**, *32*, 101090. [CrossRef]
17. Bhandari, L.; Gaur, V. Different post-processing methods to improve fatigue properties of additively built Ti-6Al-4V alloy. *Int. J. Fatigue* **2023**, *176*, 107850. [CrossRef]
18. Sanaei, N.; Fatemi, A. Analysis of the effect of surface roughness on fatigue performance of powder bed fusion additive manufactured metals. *Theor. Appl. Fract. Mech.* **2020**, *108*, 102638. [CrossRef]
19. Solberg, K.; Berto, F. The effect of defects and notches in quasi-static and fatigue loading of Inconel 718 specimens produced by selective laser melting. *Int. J. Fatigue* **2020**, *137*, 105637. [CrossRef]

20. Witkin, D.B.; Patel, D.; Albright, T.V.; Bean, G.E.; McLouth, T. Influence of surface conditions and specimen orientation on high cycle fatigue properties of Inconel 718 prepared by laser powder bed fusion. *Int. J. Fatigue* **2020**, *132*, 105392. [CrossRef]
21. Li, D.; Zhang, X.; Qin, R.; Xu, J.; Yue, D.; Chen, B. Influence of processing parameters on AlSi10Mg lattice structure during selective laser melting: Manufacturing defects, thermal behavior and compression properties. *Opt. Laser Technol.* **2023**, *161*, 109182. [CrossRef]
22. Li, D.; Qin, R.; Chen, B.; Zhou, J. Analysis of mechanical properties of lattice structures with stochastic geometric defects in additive manufacturing. *Mater. Sci. Eng. A* **2021**, *822*, 141666. [CrossRef]
23. Park, M.; Venter, M.P.; Du Plessis, A. A lattice structure coupon sample for build quality control in metal additive manufacturing. *Mater. Des.* **2023**, *235*, 112436. [CrossRef]
24. Hyer, H.; Zhou, L.; Park, S.; Gottsfritz, G.; Benson, G.; Tolentino, B.; McWilliams, B.; Cho, K.; Sohn, Y. Understanding the laser powder bed fusion of AlSi10Mg alloy. *Metallogr. Microstruct. Anal.* **2020**, *9*, 484–502. [CrossRef]
25. Zhang, J.; Song, B.; Wei, Q.; Bourell, D.; Shi, Y. A review of selective laser melting of aluminum alloys: Processing, microstructure, property and developing trends. *J. Mater. Sci. Technol.* **2019**, *35*, 270–284. [CrossRef]
26. Li, C.; Liu, D.; Liu, G.; Liu, S.; Jin, X.; Bai, Y. Surface characteristics enhancement and morphology evolution of selective-laser-melting (SLM) fabricated stainless steel 316L by laser polishing. *Opt. Laser Technol.* **2023**, *162*, 109246. [CrossRef]
27. Cao, L.; Li, J.; Hu, J.; Liu, H.; Wu, Y.; Zhou, Q. Optimization of surface roughness and dimensional accuracy in LPBF additive manufacturing. *Opt. Laser Technol.* **2021**, *142*, 107246. [CrossRef]
28. La Fé-Perdomo, I.; Ramos-Grez, J.; Mujica, R.; Rivas, M. Surface roughness Ra prediction in Selective Laser Melting of 316L stainless steel by means of artificial intelligence inference. *J. King Saud Univ. Eng. Sci.* **2023**, *35*, 148–156.
29. Wang, X.; Muñiz-Lerma, J.A.; Sánchez-Mata, O.; Shandiz, M.A.; Brochu, M. Microstructure and mechanical properties of stainless steel 316L vertical struts manufactured by laser powder bed fusion process. *Mater. Sci. Eng. A* **2018**, *736*, 27–40. [CrossRef]
30. Dong, Z.; Zhang, X.; Shi, W.; Zhou, H.; Lei, H.; Liang, J. Study of size effect on microstructure and mechanical properties of AlSi10Mg samples made by selective laser melting. *Materials* **2018**, *11*, 2463. [CrossRef]
31. Majeed, A.; Ahmed, A.; Liu, B.; Ren, S.; Yang, J. Influence of wall thickness on the hardness of AlSi10Mg alloy parts manufactured by selective laser melting. *Procedia CIRP* **2019**, *81*, 459–463. [CrossRef]
32. Liang, H.; Xie, D.; Mao, Y.; Shi, J.; Wang, C.; Shen, L.; Tian, Z. The size effect on forming quality of Ti–6Al–4V solid struts fabricated via laser powder bed fusion. *Metals* **2019**, *9*, 416. [CrossRef]
33. Sombatmai, A.; Uthaisangsuk, V.; Wongwises, S.; Promoppatum, P. Multiscale investigation of the influence of geometrical imperfections, porosity, and size-dependent features on mechanical behavior of additively manufactured Ti-6Al-4V lattice struts. *Mater. Des.* **2021**, *209*, 109985. [CrossRef]
34. Barba, D.; Alabort, C.; Tang, Y.T.; Viscasillas, M.J.; Reed, R.C.; Alabort, E. On the size and orientation effect in additive manufactured Ti-6Al-4V. *Mater. Des.* **2020**, *186*, 108235. [CrossRef]
35. Shahabad, S.I.; Ali, U.; Zhang, Z.; Keshavarzkermani, A.; Esmaeilizadeh, R.; Bonakdar, A.; Toyserkani, E. On the effect of thin-wall thickness on melt pool dimensions in laser powder-bed fusion of Hastelloy X: Numerical modeling and experimental validation. *J. Manuf. Process.* **2022**, *75*, 435–449. [CrossRef]
36. Promoppatum, P.; Taprachareon, K.; Chayasombat, B.; Tanprayoon, D. Understanding size-dependent thermal, microstructural, mechanical behaviors of additively manufactured Ti-6Al-4V from experiments and thermo-metallurgical simulation. *J. Manuf. Process.* **2022**, *75*, 1162–1174. [CrossRef]
37. Zhao, L.; Song, L.; Macías, J.G.S.; Zhu, Y.; Huang, M.; Simar, A.; Li, Z. Review on the correlation between microstructure and mechanical performance for laser powder bed fusion AlSi10Mg. *Addit. Manuf.* **2022**, *56*, 102914. [CrossRef]
38. *GB/T 20975.10-2020[S]*; Methods for Chemical Analysis of Aluminium and Aluminium Alloys. Standardization Administration of China: Beijing, China, 2020.
39. Minkowitz, L.; Arneitz, S.; Effertz, P.S.; Amancio-Filho, S.T. Laser-powder bed fusion process optimisation of AlSi10Mg using extra trees regression. *Mater. Des.* **2023**, *227*, 111718. [CrossRef]
40. Snell, R.; Tammas-Williams, S.; Chechik, L.; Lyle, A.; Hernández-Nava, E.; Boig, C.; Panoutsos, G.; Todd, I. Methods for rapid pore classification in metal additive manufacturing. *JOM* **2020**, *72*, 101–109. [CrossRef]
41. Nandhakumar, R.; Venkatesan, K. A process parameters review on Selective laser melting-based additive manufacturing of Single and Multi-Material: Microstructure, Properties, and machinability aspects. *Mater. Today Commun.* **2023**, *35*, 105538. [CrossRef]
42. Kumar, P.; Farah, J.; Akram, J.; Teng, C.; Ginn, J.; Misra, M. Influence of laser processing parameters on porosity in Inconel 718 during additive manufacturing. *Int. J. Adv. Manuf. Technol.* **2019**, *103*, 1497–1507. [CrossRef]
43. Wang, S.; Ning, J.; Zhu, L.; Yang, Z.; Yan, W.; Dun, Y.; Xue, P.; Bose, S.; Bandyopadhyay, A. Role of porosity defects in metal 3D printing: Formation mechanisms, impacts on properties and mitigation strategies. *Mater. Today* **2022**, *59*, 133–160. [CrossRef]
44. Hojjatzadeh, S.M.H.; Parab, N.D.; Guo, Q.; Qu, M.; Xiong, L.; Zhao, C.; Escano, L.; Kamel, F.; Everhart, W.; Sun, T.; et al. Direct observation of pore formation mechanisms during LPBF additive manufacturing process and high energy density laser welding. *Int. J. Mach. Tools Manuf.* **2020**, *153*, 103555. [CrossRef]

45. Martin, A.A.; Calta, N.P.; Khairallah, S.A.; Wang, J.; Depond, P.J.; Fong, A.Y.; Thampy, V.; Guss, G.M.; Kiss, A.M.; Stone, K.H.; et al. Dynamics of pore formation during laser powder bed fusion additive manufacturing. *Nat. Commun.* **2019**, *10*, 1987. [CrossRef]
46. Dong, Z.; Liu, Y.; Li, W.; Liang, J. Orientation dependency for microstructure, geometric accuracy and mechanical properties of selective laser melting AlSi10Mg lattices. *J. Alloys Compd.* **2019**, *791*, 490–500. [CrossRef]